

See discussions, stats, and author profiles for this publication at: <https://www.researchgate.net/publication/260792844>

Temperature-Dependent Morphology Evolution and Surface Plasmon Absorption of Ultrathin Gold Island Films

ARTICLE in THE JOURNAL OF PHYSICAL CHEMISTRY C · APRIL 2012

Impact Factor: 4.77 · DOI: 10.1021/jp300260h

CITATIONS

36

READS

58

5 AUTHORS, INCLUDING:



[Hongtao Sun](#)

University of California, Los Angeles

36 PUBLICATIONS 775 CITATIONS

[SEE PROFILE](#)



[Mingpeng Yu](#)

Tsinghua University

37 PUBLICATIONS 639 CITATIONS

[SEE PROFILE](#)



[Gongkai Wang](#)

Hebei University of Technology

22 PUBLICATIONS 425 CITATIONS

[SEE PROFILE](#)



[Xinde Sun](#)

East China Normal University

85 PUBLICATIONS 1,382 CITATIONS

[SEE PROFILE](#)

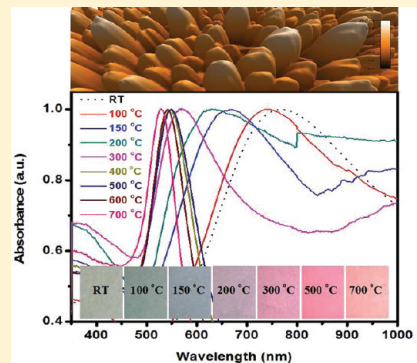
Temperature-Dependent Morphology Evolution and Surface Plasmon Absorption of Ultrathin Gold Island Films

Hongtao Sun, Mingpeng Yu, Gongkai Wang, Xiang Sun, and Jie Lian*

Department of Mechanical, Aerospace & Nuclear Engineering, Rensselaer Polytechnic Institute, Troy, New York 12180, United States

 Supporting Information

ABSTRACT: Ultrathin gold island films on transparent substrates display a characteristic surface plasmon (SP) absorption band in which the peak position and full width at half-maximum (fwhm) are highly sensitive to the film morphology. In the present study, we investigated the temperature dependence of morphological evolution and the corresponding unique surface plasmon resonance (SPR) properties variation of the ultrathin gold island films (5 nm nominal thickness) upon rapid thermal annealing for 180 s at different temperatures ranging from 100 to 700 °C. The morphological evolution of the ultrathin gold film upon the thermal annealing-induced dewetting was studied using scanning electron microscopy (SEM) and atomic force microscopy (AFM), and the optical properties variation was characterized by a transmission UV-vis-NIR spectroscopy. A strong temperature dependence of morphological evolution and optical properties variation as a function of thermal treatment conditions was identified. The blue shift and band narrowing of the SP absorption band can be correlated with various morphological characteristics, e.g., the increased open area fraction of island films, average separation between islands or nanoparticles (NPs) and the decreased aspect ratio (length divided by width) upon increasing thermal treatment temperatures. The temperature dependence of the transmission localized surface plasmon resonance (T-LSPR) may enable a science-based design of optical sensing and dynamic thermal sensors upon the morphological manipulation of ultrathin metallic surface nanostructures by thermal dewetting.



1. INTRODUCTION

Metallic nanostructures including nanofilms and nanoparticles (NPs) have been widely used in many applications including advanced sensing and catalytic systems based on their unique optical and catalytic properties. For example, noble metals such as gold and silver on transparent substrates are used for T-LSPR sensing. The optical property and sensing capability can be tailored by manipulating the organization of the metal films, e.g., through patterning nanoparticle arrays by lithography,^{1,2} and controlling thin island film morphologies upon the evaporation and deposition processes.^{3–5} Ultrathin gold island films evaporated onto transparent substrates show the surface plasmon (SP) band in which the wavelength of maximum absorbance and intensity and its fwhm are highly dependent on island film morphologies.^{4,6–13} The sensing capability and limits of the T-LSPR based sensors are generally determined by refractive index sensitivity (RIS) in terms of SP absorption band shift and plasmon intensity change (PIC) per refractive index unit (RIU).^{7,8}

In addition, noble metal thin island films have also been widely used in SERS spectroscopy and infrared spectroscopy based on the enhancement of the local electromagnetic field that leads to a dramatic increase in the cross-section of the scattering near the metal island film.^{14,15} One of the main contributions to the strong enhancement of the local electromagnetic field is due to surface plasmons in resonance

with excitation and scattered fields. In the development of catalysts, gold catalysts have been exploited for many commercial applications¹⁶ and have opened up new opportunities in green technology¹⁷ in which the particle size and the support properties are crucial to their catalytic properties.^{18–22} For example, small sized gold-based catalysts (e.g., less than 8 nm in diameter) become active in a small amount and at lower temperature (even lower than room temperature), useful for addressing the cold-startup problem of an engine.^{18,23,24} Therefore, the morphological control and tuning of the optical properties are critical for the applications of metallic nanostructures used as advanced sensing and catalytic systems.

Ultrathin films may form far from the equilibrium with respect to discrete particles with high surface-to-volume ratios. Upon thermal treatment, ultrathin metal films deposited on nonwetted substrates may be energetically metastable and can develop holes and eventually disintegrate into an array of sphere-shaped particles with a lower surface-to-volume ratio. This process is referred to as solid-state dewetting, which can generally occur well below melting temperature, and thus, the ultrathin island film nanostructures have a large driving force to reduce the surface area in order to minimize the total energy of

Received: January 9, 2012

Revised: March 13, 2012

Published: March 23, 2012



Table 1. Statistical Analysis of Morphology and Optical Properties for 5 nm Gold Thin Island Films upon Different Thermal Treatment Temperatures for 180 s

temp (°C)	a ^a (nm)	b ^b (nm)	c ^c (nm)	open area fraction (%)	aspect ratio	circularity	roughness (nm)	SPB (nm)	fwhm (nm)
23	44 ± 49	23 ± 21	5 ± 1	36.9	1.95 ± 1.22	0.40 ± 0.19	1.10 ± 0.92	771	460
100	53 ± 42	25 ± 20		43.0	2.00 ± 1.98	0.48 ± 0.25		741	389
150	39 ± 23	21 ± 10	7 ± 1	52.0	1.99 ± 1.46	0.59 ± 0.26	1.30 ± 1.01	665	304
200	54 ± 41	28 ± 23	11 ± 1	55.7	2.09 ± 2.09	0.36 ± 0.27	3.04 ± 2.36	627	498
300	47 ± 28	26 ± 14	13 ± 2	61.9	1.87 ± 1.03	0.68 ± 0.24	4.59 ± 3.71	569	142
400	28 ± 12	19 ± 6	14 ± 2	64.5	1.49 ± 0.47	0.83 ± 0.14	4.33 ± 3.57	548	95
500	29 ± 13	20 ± 7	15 ± 3	65.8	1.45 ± 0.47	0.84 ± 0.11	5.43 ± 4.34	550	80
600	30 ± 12	20 ± 8	19 ± 2	66.5	1.53 ± 0.43	0.78 ± 0.13	7.14 ± 5.76	542	63
700	32 ± 11	20 ± 6	17 ± 2	68.3	1.57 ± 0.41	0.83 ± 0.12	6.25 ± 5.11	529	50

^aIsland or nanoparticle length. ^bIsland or nanoparticle width. ^cIsland or nanoparticle height.

the system. When such a material is in contact with a nonwetted substrate, the energy minimized shape is a spherical cap. Dewetting typically starts with the formation of metastable holes and continues to evolve into the equilibrium shape via growth of the holes by various mechanisms, such as nucleation of vacancies at grain boundaries and grain boundary triple junction in areas of high local stress²⁵ or at the interface between film and substrate.^{26–28}

The energy minimization process of the ultrathin metal film upon thermal dewetting-induced morphological instability represents an effective approach for tuning the optical and catalytic properties through the manipulation of morphology and self-organization of the metallic surface nanostructures. For example, gold thin films evaporated on silanized glass and annealed 20 h at low temperature (200 °C) or evaporated on bare glass and annealed 10 h at high temperature (550–600 °C) showed a strong dependence of the localized SP band on the morphology of the films.^{6,8,9}

On the other hand, based on the variation of the characteristic optical properties, the morphological evolution of metallic films on nonwetted substrates upon thermal dewetting can also be characterized by spectroscopic techniques such as localized surface plasmon resonance (LSPR) spectroscopy,^{29,30} infrared spectroscopy,^{31–33} and surface-enhanced Raman scattering (SERS) spectroscopy.^{34–36} Particularly, interaction of an incident electromagnetic wave with the collective oscillation of the conduction electrons of nanostructures of noble metals shows a LSPR, resulting in strong scattering with a distinct SP absorption band. The frequency and intensity of the SP band are characteristics of materials and highly dependent on morphological characteristics such as particle size, size distribution, shape, and spacing of the nanostructures, as well as dielectric constants of the surrounding medium.^{37,38} The variations of the dielectric constant in the environment^{2,3,37,39–42} and SP coupling^{43–46} can be recorded by the sensors based on LSPR and thus can be employed as optical sensors for chemical^{40,47–49} and biological^{50–55} sensing applications.

In the present work, we prepared ultrathin gold island films with the nominal thickness of 5 nm by thermal evaporation on bare quartz slides offering a smooth transparent substrate and investigated the temperature dependence of the morphological evolution and optical properties variation induced by thermal dewetting. The prepared ultrathin Au films were treated by rapid heating at temperatures of 100–700 °C for 180 s. The morphology evolution was characterized using high resolution imaging techniques such as SEM and AFM, and the optical response of ultrathin gold island films was measured using

UV-vis-NIR spectroscopy. The correlation among the surface morphological evolution, optical properties tuning, and the corresponding thermal treatment conditions was established, enabling the design of advanced sensor and catalytic systems upon the manipulation of metallic surface nanostructures.

2. EXPERIMENTAL METHODS

2.1. Ultrathin Gold Island Film Preparation. Quartz slides ($12 \times 12 \text{ mm}^2$) were rinsed with acetone, ethanol, and deionized water, in an ultrasonic bath for 15 min and dried under a nitrogen stream. Gold (99.95%, Alfa Aesar, USA) was evaporated from a tungsten boat at around 1.8×10^{-6} Torr, at a deposition rate of $0.017\text{--}0.083 \text{ nm s}^{-1}$ in a high vacuum thermal evaporator. The nominal thickness of ultrathin gold island films is around 5.0 nm.

2.2. Thermal Treatment of As-Prepared Ultrathin Gold Island Films. Thermal treatment of the ultrathin gold island film coated on quartz substrates was carried out in air by laying samples in a tube furnace at various temperatures ranging from 100 to 700 °C for 180 s and retracted to cool down in air to room temperature before any measurements.

2.3. UV-vis-NIR Spectroscopy. Optical measurements were carried out in air after thermal treatment using a Varian Cary UV-vis-NIR spectrophotometer with a scan rate of 600 nm min^{-1} , 1 nm interval, and 0.1 s average measurement time per point. A baseline correction procedure was implemented prior to each measurement. The SP absorption band of the 5 nm nominal thickness gold island film is located on a 760 nm wavelength prior to rapid thermal treatment.

2.4. Atomic Force Microscopy (AFM). Morphological and topological variations of the ultrathin gold films upon thermal treatment were characterized by a MFP-3D AFM operated in the acoustic AC mode (tapping mode). The cantilever used was AC240TS series of silicon with a resonant frequency of 50–90 kHz and an average tip radius of $9 \pm 2 \text{ nm}$.

2.5. High-Resolution Scanning Electron Microscopy (HR-SEM). Images were obtained using a Carl Zeiss Supra SEM with a field emission electron source. The SEM measurement was performed at a low energy (voltage, 0.5–2.0 kV; aperture size (current), 10 μm) with a working distance of around 4 mm in order to reduce the charging effect. Statistical analysis of the morphological data based on HR-SEM images was derived from the ImageJ image processing software and was included in Table 1.

2.6. XRD Measurements. Five nanometer thick gold island films upon thermal treatment were characterized using a Philips X'Pert Pro diffractometer with a scan range of $30\text{--}60^\circ$ and 25 s per step. To determine the fwhm of the Au peak, the diffraction

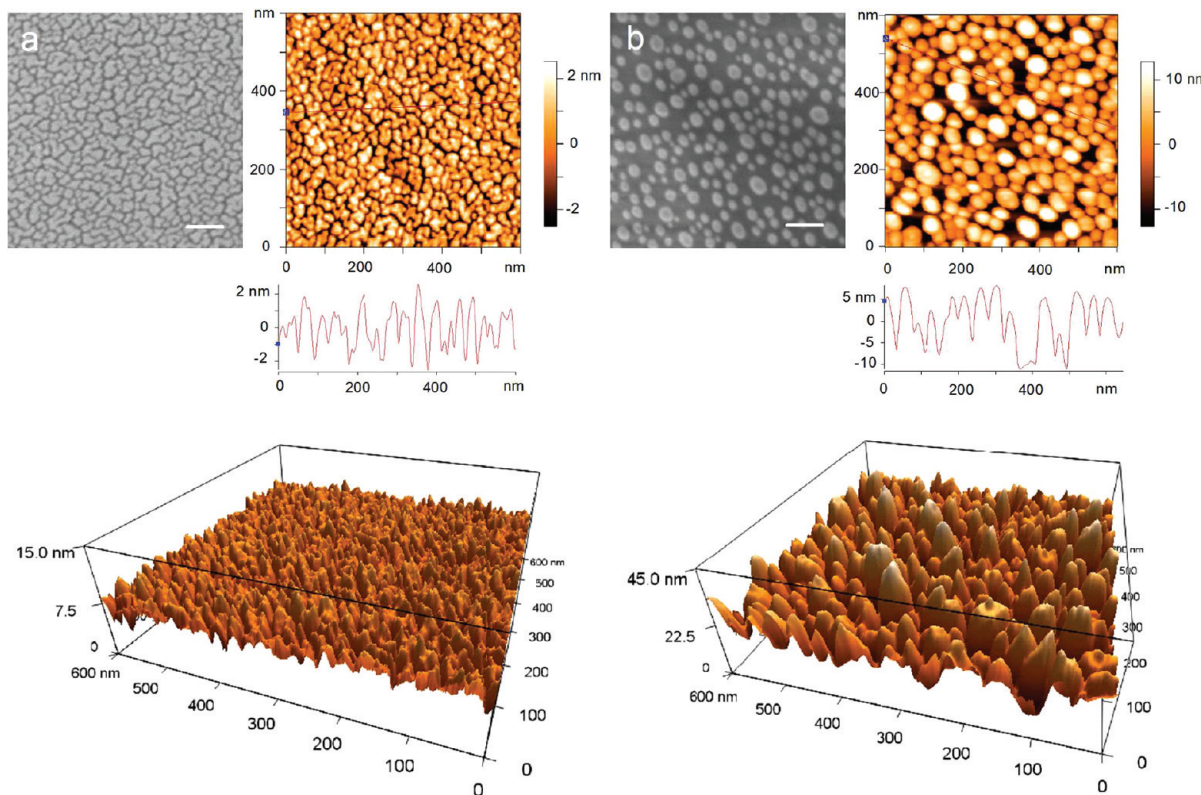


Figure 1. HR-SEM and AC mode AFM images showing the morphology and topology of ultrathin gold island films evaporated on quartz with the nominal thickness of 5 nm: (a) prior to thermal treatment; and (b) upon 700 °C thermal treatment for 180 s. Scale bars represent 100 nm in HR-SEM images. A typical cross-section profile analysis is shown below each AFM image with different z scales.

peak was identified and fitted using a Gaussian function. The mean value and the error of the fwhm were directly derived as well. The average grain size of the gold surface nanostructure was calculated based on the Debye–Scherrer formula (β : fwhm; θ : half 2-theta value)

$$D_p = \frac{0.9\lambda}{\beta \cos \theta} \quad (1)$$

3. RESULTS AND DISCUSSION

3.1. Morphology of Gold Island Films. Figure 1 shows HR-SEM and AFM images of gold island films with the nominal thickness of 5.0 nm before and after thermal treatment at 700 °C for 180 s. The ultrathin island film prior to thermal treatment displays an irregular and complex shape formed during the high vacuum evaporation process in which the gold NPs are nucleated and coalesced on the quartz substrate to form a partially connected island film. Upon the thermal treatment, the island film experienced a drastic shape change varying with the heating temperature. The drastic shape change is caused by the thermal dewetting-induced morphological instability of the ultrathin gold film deposited on the nonwetted quartz substrate, as driven by the surface diffusion to reduce the surface area in order to minimize the total energy of the system. Upon rapid thermal annealing, the dewetted pattern appeared in which the partially connected island films became discontinuous upon hole nucleation and eventually disintegrated into isolated sphere-shaped particles with a lower surface-to-volume ratio, as shown in Figure 1b.

In order to investigate thermal-induced morphology evolution in details, HR-SEM and AFM were used to provide

a full 3-dimensional description of 5 nm gold island films during a series of thermal treatments (100 to 700 °C) for 180 s. In the low temperature regime with the annealing temperature increased from room temperature (Figure 1a) to 150 °C (Figure 2a), gold island films became less connected, and gold island coverage decreased due to the enlarged interisland spacing and island height. For 200 °C thermal treatment shown in Figure 2b, island films were elongated into anisotropic worm-like island films and necking formed between adjacent islands resulting in a very irregular pattern with a large particle aspect ratio (as defined by the island length divided by its width) roughly ranging from 1 to more than 3. It is due to the nonuniform thickness of the island film structure, thus faster surface diffusion occurred in the thinner regions. With further increasing in the heating temperature (300 °C), the worm-like gold islands evolved into more regularly isotropic NPs from round to elliptical shapes as shown in Figure 2c by thermal-induced dewetting to minimize the total energy of the system. All the worm-like island films have been reshaped into isotropic nanostructured particles (the energy minimized shape) upon 400 °C thermal treatment as shown in Figure 2d. Further heated at 500 °C (Figure 2e), small NPs coalesced into larger sized particles of isotropic nanospheres at 600 °C in Figure 2f as compared to the sphere particles formed at 400 °C.

Concurrent with the morphological variation of the ultrathin gold film upon thermal dewetting, the average size of individual islands and the space (separation distance) between islands increase consistently from thin island films to isolated NPs. The islands were also reshaped from anisotropic worm-like islands to isotropic round-shaped NPs. The vertical dimension (height) of gold islands or NPs was obtained from the

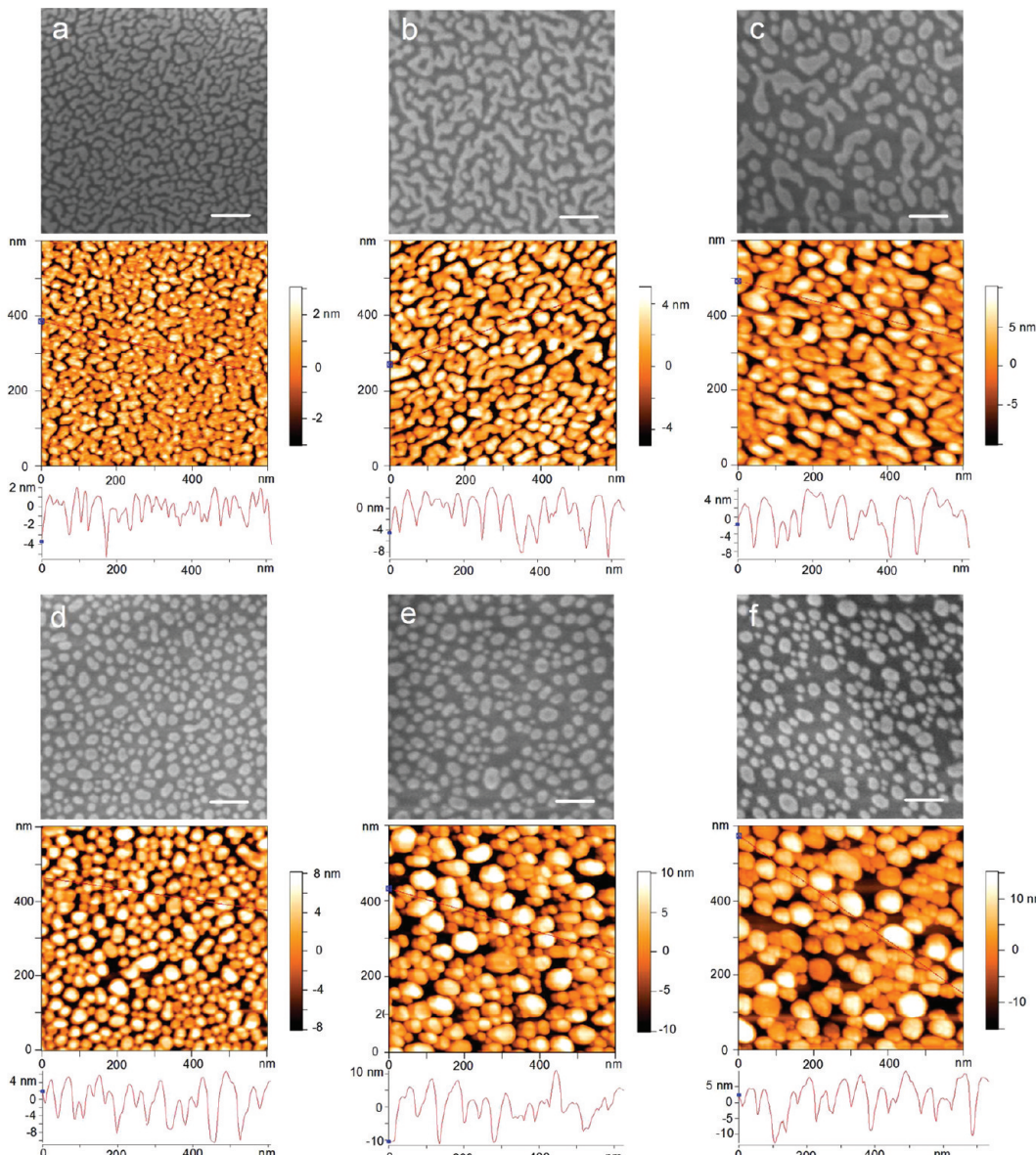


Figure 2. HR-SEM and AC mode AFM images of 5 nm gold island films evaporated on quartz upon different thermal treatment for 180 s: 150 °C (a); 200 °C (b); 300 °C (c); 400 °C (d); 500 °C (e); and 600 °C (f). Scale bars represent 100 nm in HR-SEM images. A typical cross-section profile analysis is shown below each AFM image with different *z* scales.

topographical profile based on the cross-sectional analysis of the AFM images as shown below each AFM image with different *z* scales. The island height continuously increases with the heating temperature, from 5 ± 1 nm at room temperature to 19 ± 2 nm at 600 °C. The gold islands appear larger in size and closer in spacing as determined from the AC mode AFM images as compared with those in corresponding HR-SEM, resulting from the convolution of AFM probes. Therefore, the island or NP dimensions determined by HR-SEM images are more reliable than by AFM images; while AFM can provide more information on the island height.

XRD measurements were also performed to follow the thermal-induced dewetting process and determine the structural variation of films. As showed in Figure 3a (blue circle represents the peak from the quartz substrate; orange diamond represents the peak from gold island films), the intensity and width of gold peaks gradually increase showing a strong {111} texture with increased heating temperatures.

The average grain size of ultrathin gold island films determined from XRD based on the Debye–Scherrer formula increases with the heating temperature, consistent with the increasing height of islands or NPs as obtained from AFM images, as shown in Figure 3b. The combination of the HR-SEM, AFM, and XRD allow a reliable description of the 3-dimensional morphology, topography, and structure evolution of the ultrathin gold film upon thermal treatment.

Statistical analysis of the HR-SEM images was conducted using the ImageJ image processing software, in which the islands or NPs were selected by adjusting the threshold image intensity, and thus to quantitatively estimate the gold film coverage, aspect ratio, circularity, and dimensions. The gold area fraction (area coverage) as shown in Figure 4a decreases gradually with increased thermal treatment temperatures, consistent with the fact that thermal dewetting leads to the coalescence of adjacent islands with increased island height and interisland spacing. Figure 4b shows the variation of average

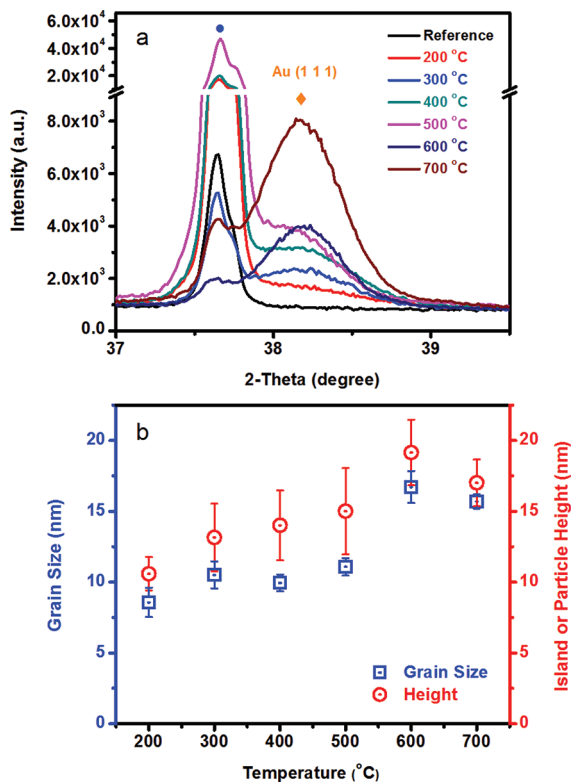


Figure 3. (a) XRD patterns of 5 nm ultrathin gold island films upon 200 to 700 °C thermal treatment for 180 s. Blue circle, quartz peak; orange diamond, gold peak. (b) The correlation among the gold grain size estimated using the Scherrer equation based on XRD measurements, gold island or particle height obtained from AFM images and the thermal treatment temperature.

island areas assuming a spherical feature as a function of the heating temperature. The island area initially shows an increasing trend resulting from joining adjacent worm-like islands at the low temperature regime (RT–200 °C). With further increase in temperature from 200 to 400 °C, the worm-like gold islands change their shapes into more regularly defined and isotropic NPs from round to elliptical shapes upon thermal-dewetting in order to minimize the total energy in the system thus decreasing the island area. At higher temperatures (400–700 °C), small spheres coalesce into larger sized and more isotropic spheres, and the average island area increases slightly. The thermal dewetting-induced height variation of island films as obtained from AFM is in reasonable agreement with the variation trend of the average island length and width and enhanced circularity of the geometry in Table 1 based on SEM measurements.

The mean value and its standard deviation of the statistical distribution of gold island aspect ratios are tabulated in Table 1 and Figure S1, Supporting Information, for the whole temperature range. The cumulative probability (the probability that a random variable is less than or equal to a specified value) was analyzed, as shown in Figure 5 and the histograms were shown in Figure S1 of the Supporting Information. More than 95% of the islands for the high temperature range (400–700 °C) and more than 80% of the islands for the low temperature range (RT–300 °C) have an aspect ratio lower than 2, except at 200 °C. Additionally, more than 80% of the islands for the high temperature range have an aspect ratio lower than 1.5,

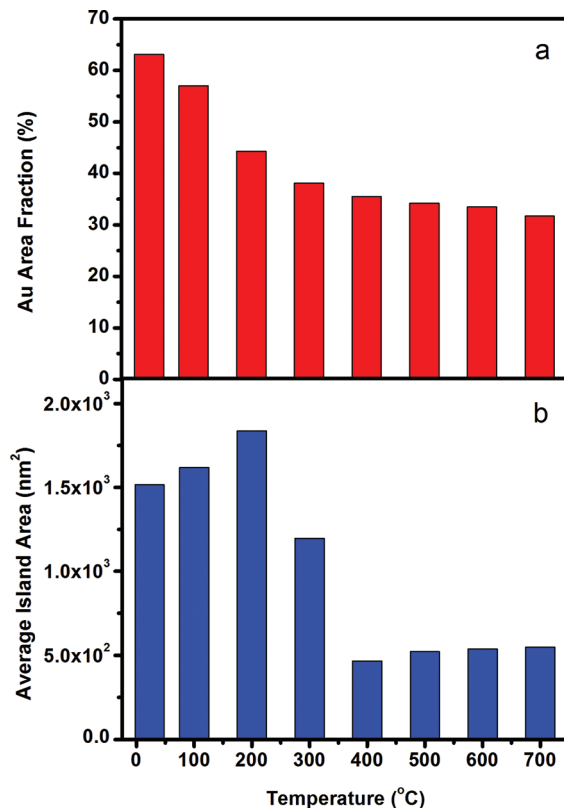


Figure 4. (a) Gold islands coverage on the quartz substrate versus the thermal treatment temperature. (b) Average gold island area versus the thermal treatment temperature.

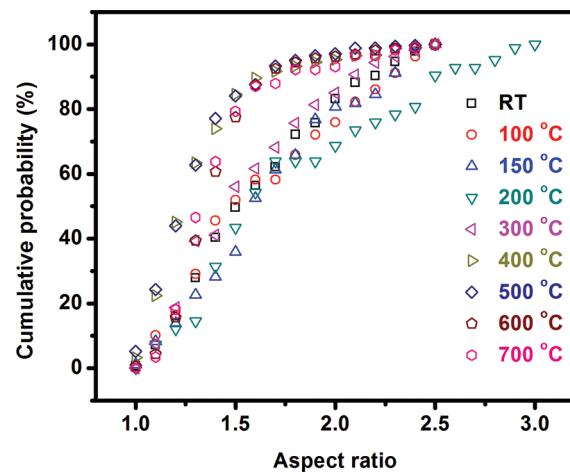


Figure 5. Cumulative probability (the probability that a random variable is less than or equal to a specified value) of the aspect ratio (length divided by width) of gold islands upon various thermal treatment temperatures ranging from 100 to 700 °C. The aspect ratios were extracted from HR-SEM images using imageJ image processing software.

suggesting a more isotropic morphology of the gold NPs upon thermal dewetting at a greater thermal treatment temperature.

3.2. Optical Properties of Gold Island Films upon Various Thermal Treatment Temperatures. The drastic morphological and topographical variations of the ultrathin gold film upon thermal dewetting significantly alter the optical properties as characterized by the T-LSPR spectroscopy, monitoring changes in the SP absorption band and its fwhm

in the visible spectral range. Figure 6a shows UV-vis spectra of ultrathin gold island films upon 100 to 700 °C thermal

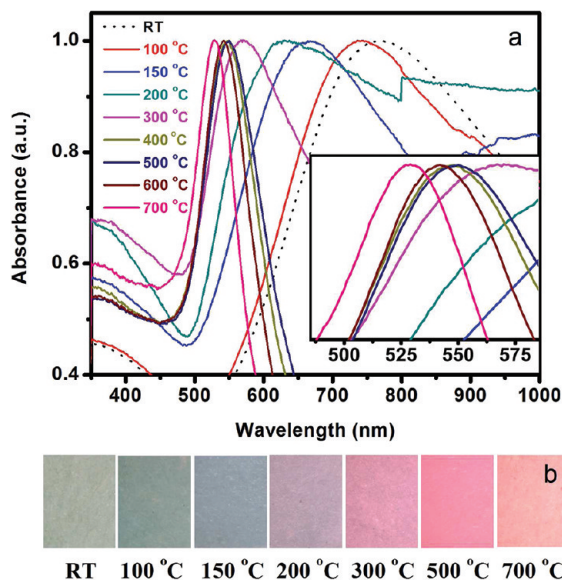


Figure 6. (a) UV-vis-NIR spectra of 5 nm ultrathin gold island films evaporated on bare quartz upon various thermal treatments from 100 to 700 °C for 180 s. Inset is a close-up image showing the blue shift of the surface plasmon peak of the ultrathin Au film upon thermal treatments from 300 to 700 °C; (b) Optical images of color change.

treatment for 180 s. All the UV-vis-NIR spectra illustrate a continuous blue shift attributed to the increase of the average separation between islands as shown in Figure 2 and thus a weakening of the coupling effect as increasing the thermal treatment temperature. The blue shift of the SP band is consistent with the previous studies on gold films upon more equilibrium heating (e.g., at 200 °C for 20 h or 550 °C for 10 h), and 15 and 35 nm gold NPs monolayers upon various heating temperature for 1 h, in which the optical properties of the films or NPs are controlled by the morphological characteristics.^{6–9} The variations of the SP absorption band in UV-vis-NIR spectra also result in a distinct color change of 5 nm thick gold films upon 180 s thermal treatment from cyan at 100 °C, blue at 150 °C, purple at 200 °C, pink at 500 °C to yellowish-red at 700 °C as shown in Figure 6b.

The fwhm of the SP absorption band is affected significantly by various morphological features such as island shapes, aspect ratios and circularity, and the particle size distribution.^{4,7,8,10–13} In this study, the fwhm of the SP absorption of the ultrathin gold film upon thermal treatment decreases in general with increasing temperatures except at 200 °C. Gold islands or NPs with a lower aspect ratio and thus more isotropic shapes have a narrower SP band than those with higher aspect ratios. This is consistent with a previous study⁸ that the aspect ratio plays a dominant role in determining the fwhm of the SP band. By only considering the effect of the aspect ratio on the fwhm, gold NPs with more anisotropic features (e.g., aspect ratios greater than 2.0) display two resolved SP bands (transversal and longitudinal)^{12,56–58} due to plasmon resonance along two orientations. When decreasing the aspect ratio from 2.0 to 1.5, two bands are overlapped and combined into one broad band.¹¹ With further decrease in the aspect ratio below 1.5, the single absorption band becomes narrower with the reduced fwhm.⁵⁹ In our experiment, absorption spectra of the island

films do not exhibit two SP bands as their mean value of the aspect ratio is less than 2.0 and the majority of islands display a more isotropic shape.^{4,10,11}

It is noted that, in this study, the SP band of the 5.0 nm gold islands film heated at 200 °C has much larger fwhm, which can be well explained by their morphological characteristics. The statistic analysis of the aspect ratio as shown in Figure 5 indicates that, upon 200 °C thermal treatment, more than 30% of the islands have an aspect ratio greater than 2.0. The mean value and standard deviation as shown in Table 1 are also higher than those of the island films heated at other temperatures, resulting in a broad fwhm of the SP band. Despite that the mean value of the aspect ratio for islands is slightly larger than 2.0, the majority (more than 68%) of islands for 200 °C thermal treatment has an isotropic shape with the aspect ratio lower than 2.0 and thus only one single SP band was observed in the UV-vis-NIR spectrum.

The temperature dependent absorption maxima and the fwhm of the SP band were summarized in Figures 7a,b in which

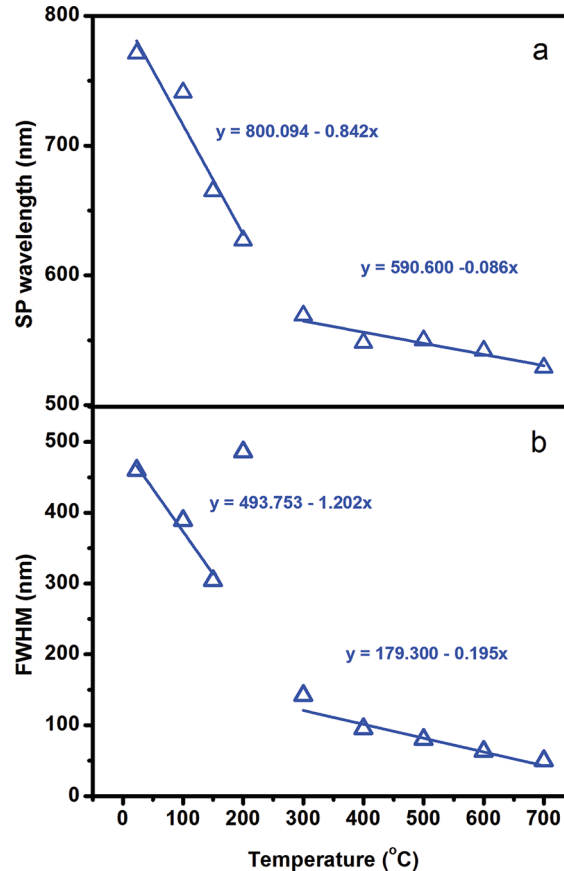


Figure 7. Temperature-dependent absorption maxima of the SP band (a) and the fwhm (b) of 5 nm ultrathin gold island films.

a continuous blue shift and SP band narrowing are clearly evidenced for the 5 nm nominal thickness Au films. The absorption maxima and its fwhm evolution in terms of temperature can be divided into two regions: low temperature (100–200 °C) and high temperature (300–700 °C) regions. The slopes of both temperature-dependent absorption maxima and fwhm are steeper in the low temperature region than that in the high temperature region, in agreement with the corresponding dramatic morphology changes showing the transition from islands to NPs.

3.3. Correlation of Thermal Dewetting-Induced Morphology Instability and Optical Properties. The correlation between the ultrathin island film morphology and its optical properties including fwhm and SP band is presented in Figures 8 and 9, respectively. Temperature-dependent fwhm

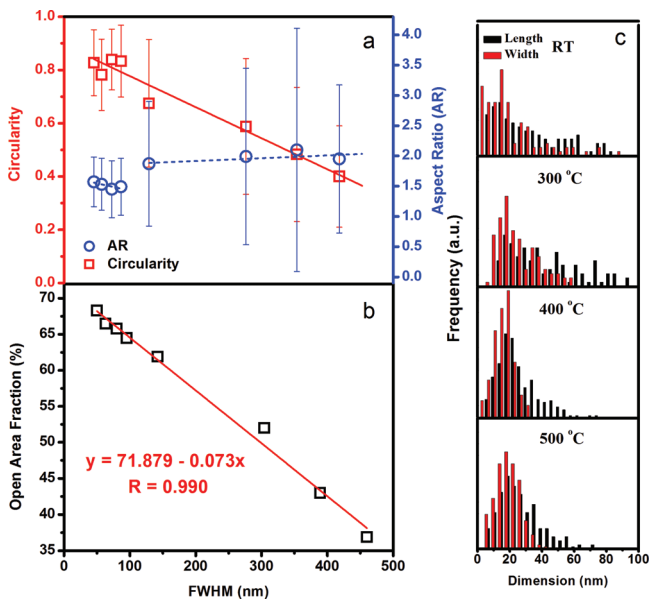


Figure 8. (a) Circularity and aspect ratio versus fwhm of the SP peak: red rectangles, circularity; blue circles, aspect ratio (AR). (b) Correlation between the spacing area fraction (%) and the fwhm of the SP peak. (c) Size distributions of gold nanoparticles or islands upon 180 s thermal treatments at different temperatures (room temperature, 300 °C, 400 °C, and 500 °C): black histogram, length of NPs or islands; red histogram, width of NPs or islands. All the statistical data were obtained from hundreds of NPs or islands in HR-SEM images and analyzed by ImageJ image processing software.

of the SP band is highly sensitive to its morphology changes. When increasing temperature, the lower aspect ratio (AR) and higher circularity by thermal-induced dewetting result in a narrowing fwhm of the SP band as shown in Figure 8a. The effect of the open (spacing) area fraction (as derived from the difference of gold area fraction from full coverage) on the SP band broadening is shown in Figure 8b. The correlation between the open area fraction and the fwhm of the SP band is almost a linear function. The size distribution is another factor that may affect the broadening of fwhm, and the length and width histogram distributions and their standard deviations based on the statistical analysis using ImageJ are included in Figure 8c and Table 1. The smaller size distribution results in a narrower SP band and smaller fwhm. Although the fwhm depends on various morphological features including circularity, open area fraction, and size distribution of gold islands or NPs, the aspect ratio and open area fraction may dominate the variation of the fwhm of the SP band.

Temperature-dependent SP band shift in Figures 6a and 7a is also highly sensitive to the morphology variations. Figure 9a shows a 99.2% R-squared linear correlation between the SP band and open area fraction of the 5 nm thick gold thin island films upon thermal treatment the temperature ranging from 100 to 700 °C for 180 s. The higher thermal treatment temperature, the larger open area fraction of the ultrathin gold film upon thermal-induced dewetting, resulting in a consistent blue shift in the SP band. Figure 9b shows the correlation

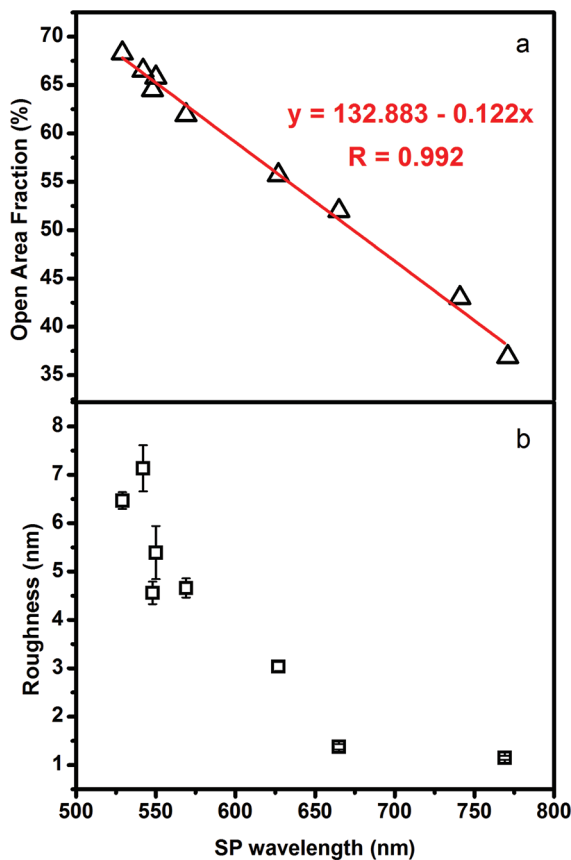


Figure 9. (a) Linear correlation between SP wavelength and spacing area fraction (%) of 5 nm ultrathin gold island films upon 100 to 700 °C thermal treatments for 180 s. (b) The correlation between SP wavelength and surface roughness obtained from AFM images.

between the surface roughness of ultrathin film as determined from AFM images and the surface plasmon absorption property. The thermal induced dewetting leads to an increase in surface roughness that results in the variations of surface resonance in the UV-vis-NIR spectra. These results clearly demonstrate the potential of using thermal treatment to manipulate the morphology of the metallic surface nanostructures to tune materials' optical properties.

4. CONCLUSIONS

In this study, thermal dewetting-induced morphological evolution and optical property of the ultrathin gold films with a 5.0 nm nominal thickness deposited on nonwetted quartz substrates were investigated upon rapid temperature heating. Their morphological, topographical, and structural variations were characterized based on the combination of HR-SEM, AFM, and XRD. The ultrathin gold island films show a strong surface resonance as characterized by vis-to-NIR absorption measurements. Upon rapid heating-induced dewetting, ultrathin gold films experience a drastic morphological evolution from a partially continuous film to a discontinuous dewetting pattern, and eventually disintegrating into isolated isotropic gold NPs. Concurrent with the morphological evolution, the particle size (length, width and height), open area fraction, and particle circularity increase accordingly. The absorption wavelength maxima and fwhms of the SP band of the ultrathin gold film are sensitive to morphological and topological variations at various thermal treatment conditions.

The blue shift and band narrowing of the SP absorption wavelength with increasing heating temperature can be attributed to the variation of the open area fraction, spacing between islands or NPs, size distribution, and the aspect ratio that may affect the coupling effects of gold islands or NPs. A near linear function is established between open area fraction and both the SP band and its fwhm. Ultrathin gold island films are highly sensitive to thermal treatment temperatures that can be easily characterized by transmission localized surface plasmon resonance (T-LSPR) spectroscopy, thus being particularly promising for the T-LSPR-based optical sensing application.

■ ASSOCIATED CONTENT

Supporting Information

Statistical distribution of aspect ratio histograms for a nominal thickness of 5 nm gold island films upon various thermal treatment temperatures. This material is available free of charge via the Internet at <http://pubs.acs.org>.

■ AUTHOR INFORMATION

Corresponding Author

*Tel: +1 5182766081. Fax: +1 5182766025. E-mail: LIANJ@rpi.edu.

Notes

The authors declare no competing financial interest.

■ ACKNOWLEDGMENTS

This work was financially supported by DOD Defense Threat Reduction Agency under the grant of HDTRA1-10-1-0002.

■ REFERENCES

- (1) Jensen, T. R.; Schatz, G. C.; Van Duyne, R. P. *J. Phys. Chem. B* **1999**, *103*, 2394–2401.
- (2) Malinsky, M. D.; Kelly, K. L.; Schatz, G. C.; Van Duyne, R. P. *J. Am. Chem. Soc.* **2001**, *123*, 1471–1482.
- (3) Kalyuzhny, G.; Vaskevich, A.; Ashkenasy, G.; Shanzer, A.; Rubinstein, I. *J. Phys. Chem. B* **2000**, *104*, 8238–8244.
- (4) Kalyuzhny, G.; Schneeweiss, M. A.; Shanzer, A.; Vaskevich, A.; Rubinstein, I. *J. Am. Chem. Soc.* **2001**, *123*, 3177–3178.
- (5) Kalyuzhny, G.; Vaskevich, A.; Schneeweiss, M. A.; Rubinstein, I. *Chem.—Eur. J.* **2002**, *8*, 3850–3857.
- (6) Doron-Mor, I.; Barkay, Z.; Filip-Granit, N.; Vaskevich, A.; Rubinstein, I. *Chem. Mater.* **2004**, *16*, 3476–3483.
- (7) Zhang, X. M.; Zhang, J. H.; Wang, H. A.; Hao, Y. D.; Zhang, X.; Wang, T. Q.; Wang, Y. N.; Zhao, R.; Zhang, H.; Yang, B. *Nanotechnology* **2010**, *21*, 465702–465712.
- (8) Karakouz, T.; Holder, D.; Goamanovsky, M.; Vaskevich, A.; Rubinstein, I. *Chem. Mater.* **2009**, *21*, 5875–5885.
- (9) Tesler, A. B.; Chuntonov, L.; Karakouz, T.; Bendikov, T. A.; Haran, G.; Vaskevich, A.; Rubinstein, I. *J. Phys. Chem. C* **2011**, *115*, 24642–24652.
- (10) Shumaker-Parry, J. S.; Rochholz, H.; Kreiter, M. *Adv. Mater.* **2005**, *17*, 2131–2134.
- (11) Sprunken, D. P.; Omi, H.; Furukawa, K.; Nakashima, H.; Sychugov, I.; Kobayashi, Y.; Torimitsu, K. *J. Phys. Chem. C* **2007**, *111*, 14299–14306.
- (12) Link, S.; El-Sayed, M. A. *J. Phys. Chem. B* **1999**, *103*, 8410–8426.
- (13) Myroshnychenko, V.; Rodriguez-Fernandez, J.; Pastoriza-Santos, I.; Funston, A. M.; Novo, C.; Mulvaney, P.; Liz-Marzan, L. M.; de Abajo, F. J. G. *Chem. Soc. Rev.* **2008**, *37*, 1792–1805.
- (14) Osawa, M.; Ataka, K.; Yoshii, K.; Nishikawa, Y. *Appl. Spectrosc.* **1993**, *47*, 1497–1502.
- (15) Gersten, J.; Nitzan, A. *J. Chem. Phys.* **1980**, *73*, 3023–3037.
- (16) Corti, C. W.; Holliday, R. J.; Thompson, D. T. *Top. Catal.* **2007**, *44*, 331–343.
- (17) Hutchings, G. J. *Catal. Today* **2007**, *122*, 196–200.
- (18) Valden, M.; Lai, X.; Goodman, D. W. *Science* **1998**, *281*, 1647–1650.
- (19) Bell, A. T. *Science* **2003**, *299*, 1688–1691.
- (20) Chen, M. S.; Goodman, D. W. *Science* **2004**, *306*, 252–255.
- (21) Valden, M.; Pak, S.; Lai, X.; Goodman, D. W. *Catal. Lett.* **1998**, *56*, 7–10.
- (22) Lim, D. C.; Lopez-Salido, I.; Dietsche, R.; Bubek, M.; Kim, Y. D. *Angew. Chem., Int. Ed.* **2006**, *45*, 2413–2415.
- (23) Haruta, M. *Catal. Today* **1997**, *36*, 153–166.
- (24) Hayashi, T.; Tanaka, K.; Haruta, M. *J. Catal.* **1998**, *178*, 566–575.
- (25) Kristensen, N.; Ericson, F.; Schweitz, J. A.; Smith, U. *Thin Solid Films* **1991**, *197*, 67–83.
- (26) Agrawal, D. C.; Raj, R. *Acta Metall. Sin.* **1989**, *37*, 2035–2038.
- (27) Kennefick, C. M.; Raj, R. *Acta Metall. Sin.* **1989**, *37*, 2947–2952.
- (28) Shaffir, E.; Riess, I.; Kaplan, W. D. *Acta Mater.* **2009**, *57*, 248–256.
- (29) Rubinstein, I.; Kalyuzhny, G.; Schneeweiss, M. A.; Shanzer, A.; Vaskevich, A. *J. Am. Chem. Soc.* **2001**, *123*, 3177–3178.
- (30) Rubinstein, I.; Lahav, M.; Vaskevich, A. *Langmuir* **2004**, *20*, 7365–7367.
- (31) Goutev, N.; Futamata, M. *Appl. Spectrosc.* **2003**, *57*, 506–513.
- (32) Niklasson, G. A.; Granqvist, C. G. *Appl. Phys. Lett.* **1985**, *46*, 713–715.
- (33) Smith, G. B. *Appl. Phys. Lett.* **1985**, *46*, 716–718.
- (34) Ye, Q.; Fang, J. X.; Sun, L. *J. Phys. Chem. B* **1997**, *101*, 8221–8224.
- (35) Tsen, M.; Sun, L. *Anal. Chim. Acta* **1995**, *307*, 333–340.
- (36) Weimer, W. A.; Gupta, R. *Chem. Phys. Lett.* **2003**, *374*, 302–306.
- (37) Underwood, S.; Mulvaney, P. *Langmuir* **1994**, *10*, 3427–3430.
- (38) Mulvaney, P. *Langmuir* **1996**, *12*, 788–800.
- (39) Englebienne, P. *Analyst* **1998**, *123*, 1599–1603.
- (40) Gluodenis, M.; Manley, C.; Foss, C. A. *Anal. Chem.* **1999**, *71*, 4554–4558.
- (41) Nath, N.; Chilkoti, A. *Anal. Chem.* **2002**, *74*, 504–509.
- (42) Sun, Y. G.; Xia, Y. N. *Anal. Chem.* **2002**, *74*, 5297–5305.
- (43) Mucic, R. C.; Storhoff, J. J.; Mirkin, C. A.; Letsinger, R. L. *J. Am. Chem. Soc.* **1998**, *120*, 12674–12675.
- (44) Reynolds, R. A.; Mirkin, C. A.; Letsinger, R. L. *J. Am. Chem. Soc.* **2000**, *122*, 3795–3796.
- (45) Storhoff, J. J.; Lazarides, A. A.; Mucic, R. C.; Mirkin, C. A.; Letsinger, R. L.; Schatz, G. C. *J. Am. Chem. Soc.* **2000**, *122*, 4640–4650.
- (46) Nath, N.; Chilkoti, A. *J. Am. Chem. Soc.* **2001**, *123*, 8197–8202.
- (47) Hutter, E.; Fendler, J. H. *Adv. Mater.* **2004**, *16*, 1685–1706.
- (48) Stewart, M. E.; Anderton, C. R.; Thompson, L. B.; Maria, J.; Gray, S. K.; Rogers, J. A.; Nuzzo, R. G. *Chem. Rev.* **2008**, *108*, 494–521.
- (49) Okamoto, T.; Yamaguchi, I.; Kobayashi, T. *Opt. Lett.* **2000**, *25*, 372–374.
- (50) Hutter, E.; Pilani, M. P. *J. Phys. Chem. B* **2003**, *107*, 6497–6499.
- (51) Larsson, E. M.; Alegret, J.; Kall, M.; Sutherland, D. S. *Nano Lett.* **2007**, *7*, 1256–1263.
- (52) Marinakos, S. M.; Chen, S. H.; Chilkoti, A. *Anal. Chem.* **2007**, *79*, 5278–5283.
- (53) Nath, N.; Chilkoti, A. *Anal. Chem.* **2004**, *76*, 5370–5378.
- (54) Jonsson, M. P.; Jonsson, P.; Dahlin, A. B.; Hook, F. *Nano Lett.* **2007**, *7*, 3462–3468.
- (55) Szunerits, S.; Praig, V. G.; Manesse, M.; Boukherroub, R. *Nanotechnology* **2008**, *19*, 195712–195718.
- (56) Kim, B.; Tripp, S. L.; Wei, A. *J. Am. Chem. Soc.* **2001**, *123*, 7955–7956.
- (57) Murphy, C. J.; San, T. K.; Gole, A. M.; Orendorff, C. J.; Gao, J. X.; Gou, L.; Hunyadi, S. E.; Li, T. *J. Phys. Chem. B* **2005**, *109*, 13857–13870.
- (58) Khlebtsov, N. G. *Quantum Electron.* **2008**, *38*, 504–529.

(59) Yu, Y. Y.; Chang, S. S.; Lee, C. L.; Wang, C. R. C. *J. Phys. Chem. B* 1997, 101, 6661–6664.